CrossMark

Observed IRIS Profiles of the h and k Doublet of Mg II and Comparison with Profiles from Quiescent Prominence NLTE Models

Jean-Claude Vial[1] · Gabriel Pelouze[1] · Petr Heinzel[2] ·
Lucia Kleint[3] · Ulrich Anzer[4]

Abstract With the launch of the *Interface Region Imaging Spectrograph* (IRIS) mission, it is now possible to obtain high-resolution solar prominence spectra and to begin to distinguish the contributions of the many (apparent or not) threads that structure prominences. We aim at comparing unique observations obtained in the Mg II h and k lines of a polar crown prominence with the radiative outputs from one-dimensional models built with non-local-thermodynamic equilibrium codes (Heinzel *et al. Astron. Astrophys.* **564**, A132, 2014). We characterize the profiles obtained through thorough calibration procedures, with attention paid to the absolute values, full-width at half-maximum, and the ratio of k to h intensities. We also show that at the top of some structures, line-of-sight velocities of about $9\,\mathrm{km\,s^{-1}}$ can be detected. We find a range of static, low-pressure, low-thickness, low-temperature models that could fit k or h observed values, but that cannot satisfy the low observed k/h ratio. We investigate whether these low values might be explained by the inclusion of horizontal flows in small-scale threads. These flows are also necessary in another class of models, where the pressure is kept low but thickness and temperature are increased up to the observed thickness and up to 15 000 K.

Keywords Mg II lines · Non-LTE diagnostic · Sun prominences · UV spectroscopy

1. Introduction

The diagnostic potential of the solar UV resonance lines of Mg II (k) at 2796.5 and 2803.65 Å (h) for studying the solar chromosphere has been known since the very beginning of the space era (*e.g.* Bonnet, Blamont, and Gildwarg, 1967; Lemaire and Skumanich, 1973;

✉ J.-C. Vial
jean-claude.vial@ias.u-psud.fr

1   Institut d'Astrophysique Spatiale, CNRS (UMR 8617) Université Paris-Sud 11, Orsay, France

2   Astronomical Institute, Czech Academy of Sciences, Ondrejov, Czech Republic

3   University of Applied Sciences and Arts Northwestern Switzerland, 5210 Windisch, Switzerland

4   Max-Planck-Institut fur Astrophysik, Garching, Germany

Springer

Doschek and Feldman, 1977). This is also true for solar prominences (filaments) since these structures have a core temperature close to the chromospheric temperature (around 10^4 K) where the h and k lines are formed (Tandberg-Hanssen, 1995). The various observations and modeling efforts during the past fourty years are described by Labrosse *et al.* (2010), Vial and Engvold (2015), and in the introduction of Heinzel, Vial, and Anzer (2014), where the latest model results are also presented in the context of the most recent observations of the *Interface Region Imaging Spectrograph* (IRIS; De Pontieu *et al.*, 2014), which performs high spatial (0.3 arcsec) and spectral (50 mÅ) resolution imaging spectroscopy in the Mg II h and k lines that has already provided unique prominence observations (Schmieder *et al.*, 2014; Heinzel *et al.*, 2015).

However, the derivation of the thermodynamic properties along with the velocity field of the observed prominences is non-trivial since it requires non-local-thermodynamic equilibrium (NLTE) radiative transfer modeling. This modeling has followed several improvements over the past 30 years from modeling one-dimensional (1D) atmospheres with crude incident radiation and scattering described by complete frequency redistribution (CRD) to modeling a set of threads with velocity fields and partial frequency redistribution (PRD) (Labrosse *et al.*, 2010). The multithread treatment with random velocities has successfully explained Lyman line profiles (asymmetries) and ratios (*e.g.* Lα/Lβ; Gunár *et al.*, 2010) , but it relies upon some hypotheses on the number and nature of the threads. Because of the lack of high spatial resolution spectroscopy, it has been impossible to derive models of individual threads from one-thread-only observations, at least within the limits of the spatial resolution. With IRIS, such a possibility now exists, and it is the purpose of this article to give an example of such observations. However, we are aware that the actual size of threads may well be at a fundamental scale much smaller than the 1000 km scale proposed by Heasley and Mihalas (1976).

We first describe the full set of observations (including some ground-based images) in Section 2, we then address the crucial issue of photometric calibration in Section 3, we describe the spatial variation of the profiles and of some parameters such as the Doppler velocity and the k/h intensity ratio in Section 4, we build and discuss representative k and h profiles, which we compare with profiles resulting from modeling in Section 5, and present complementary observations in Section 6. The conclusion is devoted to the issue of the best model(s) representative of the observations and to the efforts that need to be made to further constrain the models.

2. The IRIS and Complementary Observations

2.1. IRIS

Our observations were taken in the first days after the IRIS commissioning, and in particular, we obtained the prominence images and spectra on 18 July 2013 when the slit was in a sit-and-stare mode at a location close to the south pole. Stigmatic spectra were obtained in the Mg II channel (exposure times: 2 and 15 s) simultaneously with slit-jaw camera images (SJI) in the C II channel at 1335 Å (Figure 1). We use the "C II channel" terminology even though the filter centered at 1340 Å covers other lines and continua. The sequence of observations started at 16:10 UT but had short exposure times; consequently, we focused on the best sequence, which started at 17:26 UT and ended at 17:46 UT when a SJI image was obtained in the Mg II k line (see summary in Table 1). In Figure 1a a complex system of threads is visible, which appear to be horizontal, contrary to spicules or macrospicules. The

Table 1 IRIS Observations on 18 July 2013.

Time	SJI	Mg II h and k spectra (exposure time = 15 s)
17:26:53	1400	threads
17:27:19	2832	(prominence core)
17:27:43	2832	(threads)
17:27:53	2832	(one thread)
17:28:03	2832	(one thread)
17:28:29	1330	*
17:28:39	2832	*
17:46:07	Mg II k	

*Note that there are no observations between 17:29 and 17:46 UT.

Mg II spectra show a faint off-limb emission (Figure 1b) that is more clearly visible in the processed image of Figure 1c.

2.2. Ground-based Observatories

Simultaneous full-disk Hα images obtained at Big Bear Solar Observatory (BBSO) in California (Figure 2a) and the Teide Observatory in Tenerife (Figure 2b) also show a system of threads that are part of a prominence. As shown in Figure 5a, the out-of-limb structures are the top of a polar crown filament whose feet are located at a latitude of about 80° (taking into account the B_0 angle of $+5°$). We show here that this configuration offers a unique opportunity for separating – at least in the plane-of-sky (POS) – the components of the prominence, namely the vertical from the horizontal threads.

About 12 h after the IRIS observations, the prominence was observed with the Hα coronagraph of the Pic du Midi (Figure 3).

2.3. STEREO Observations

The thread separation is defined with the help of the *Extreme Ultraviolet Imager* (EUVI; Wuelser *et al.*, 2004) on the *Solar Terrestrial Relations Observatory* (STEREO-A and STEREO-B), separated by 80° and separated from Earth by 140° (Figure 4) and the *Atmospheric Imaging Assembly* (AIA; Lemen *et al.*, 2012) on the *Solar Dynamics Observatory* (SDO) full-Sun images obtained in He II 304 Å (Figure 5a). STEREO-A shows the feet of the prominence edge-on, while STEREO-B shows the prominence head-on, with a strong emission at the top of the threads due to line-of-sight (LOS) integration.

3. Photometric and Spectral Calibrations

Because our observations were not usual observing sequences, there are no calibrated Level 2 data available. We applied `iris_prep.pro` to the Level 1 data, which performs corrections for dark current, gain, bad pixels, and geometric and wavelength calibrations. The spectral calibration is easily performed with the help of the many absorption lines present on the disk spectra. For instance, the photospheric Mn lines at 2794.817 Å and 2801.084 Å (air wavelengths) not only provide reliable wavelength references, but also help to determine the local spectral dispersion. (At the limb, their profiles are not sensitive to the 300 s oscillations since they are mostly vertical).
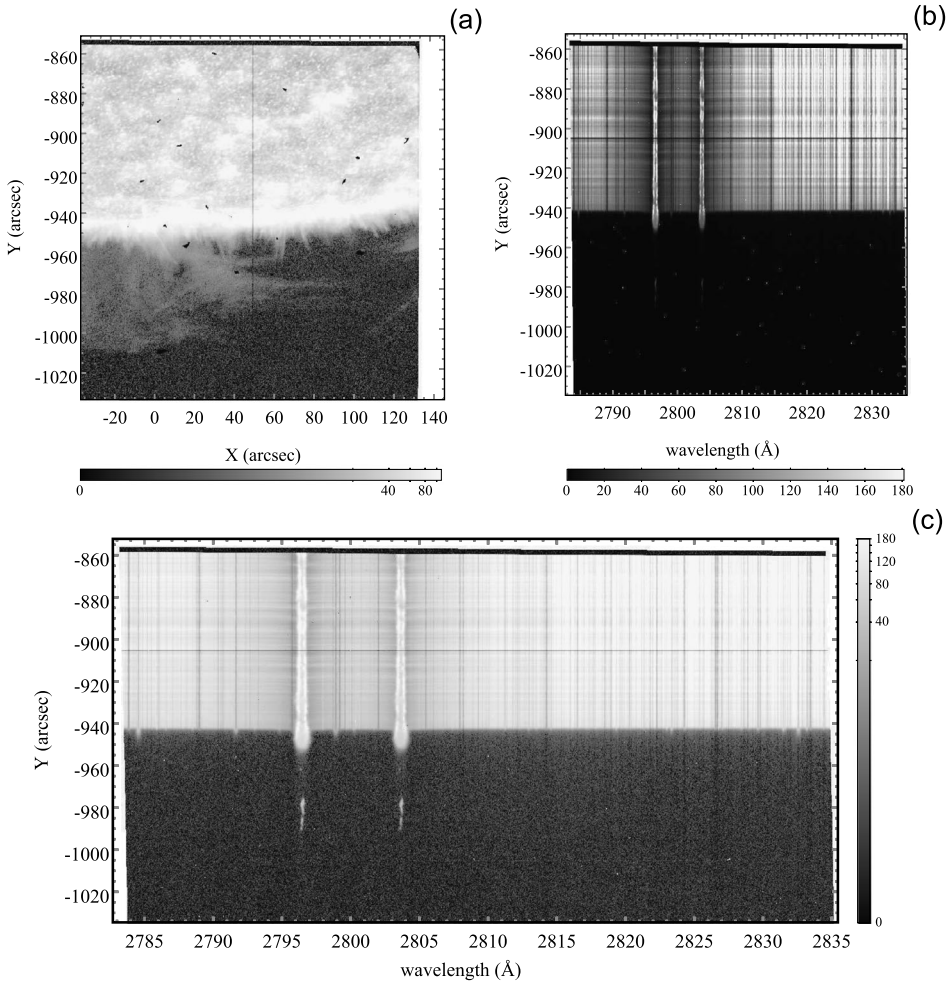
Figure 1 (a) SJI image obtained in the C II channel on 18 July 2013 at 17:28:29 (log scale). (b) Spectrum in the Mg II channel obtained on 18 July 2013 at 17:28:03 (linear scale). (c) Spectrum in the Mg II channel obtained on 18 July 2013 at 17:28:03 (log scale). All intensities are in DN.

As a first step, we used the photometric calibration, which derives from careful pre-flight calibrations performed in the laboratory (De Pontieu *et al.*, 2014) and is complemented by in-flight calibrations (*IRIS Technical Note 24*). The results of this calibration procedure are labeled as PREL, for pre-launch. However, photometric calibration is a difficult task in the UV for various reasons, one being the measurement itself, which requires a stable and well-calibrated source and/or a well-calibrated detector (see *e.g.* Huber *et al.*, 2013). Another difficulty is related to the in-flight degradation of instruments, which is not measured directly by lack of an internal (stable) source. In view of the importance of the absolute values of the intensity of the observed lines versus the comparison with intensities that result from NLTE modeling (Heinzel, Vial, and Anzer, 2014) – for instance a factor 2 in k and h intensities can result from a factor 5 in thickness for low-temperature and pressure models –, we investigated two other calibration procedures.
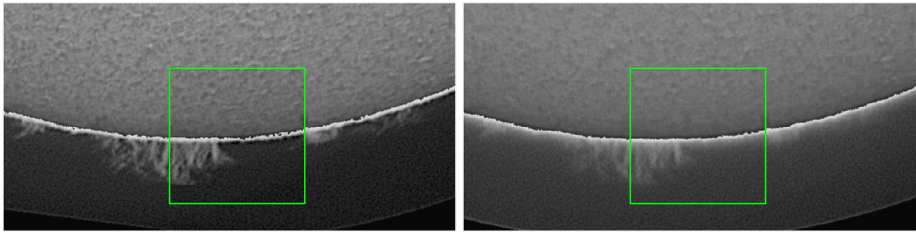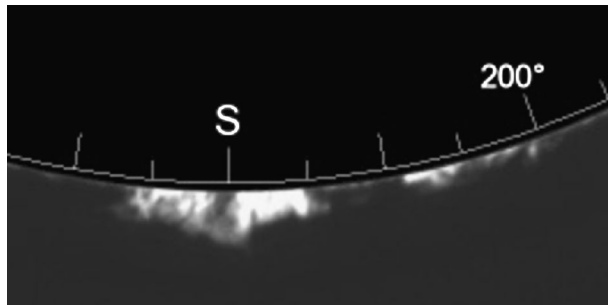
Figure 2 Hα observations on 18 July 2013. Left: BBSO at 17:29:54. Right: Teide Observatory at 17:30:14. The field of view of the SJI images of IRIS is shown as a green rectangle in both images.

Figure 3 Hα image (480 × 240 arcsec) obtained on 19 July 2013 at 5:35:20 at Pic du Midi.

As a second step, we used a different approach that consists of considering the quiet Sun as a reliable and stable source. This approach has been used in the past. For instance, Staath and Lemaire (1995) calibrated their high-resolution Mg II profiles obtained from a balloon-borne instrumentation through a comparison of their quiet-Sun (photographic) values with the calibrated (photoelectric) values of Kohl and Parkinson (hereafter KP, 1976). Similarly, Gurman (1984) compared his SMM/UVSP quiet-Sun values with KP references. More recently, Morrill and Korendyke (2008) used a combination of center-to-limb HRTS-9 (film) measurements with irradiance UARS/SUSIM and UARS/SOLSTICE measurements to derive the photometric properties of HRTS-9 and the center-to-limb intensity. They found that their quiet-Sun values, obtained in 1995 during a minimum of solar activity, were very close to the values of Kohl and Parkinson (1976) that were also obtained during a minimum of solar activity. Although our measurements took place at a (weak) peak of activity during Cycle 24, we tentatively compared our quiet-Sun measurements with those of Kohl and Parkinson (1976). These authors essentially provide intensities at different positions in the k and h profiles (from k_{1v} to h_{1r}, where k_{1v} and h_{1r} are the minima intensities in the violet and red absorption wings of the k and h lines, respectively) along with the total intensity in the integrated profiles at two solar positions (Sun center and $\mu = \cos\theta = 0.23$). IRIS performed many measurements at these two locations on the solar disk, but we chose to work on the simultaneous observations performed on the solar disk, and in particular at $\mu = 0.23$ (for details, see the the Appendix). The results from this calibration procedure are labeled KP (for Kohl and Parkinson, 1976). The comparison between the spectra calibrated with the two methods (PREL and KP) is shown in Figure 6.

It is clear that the KP values are about 30 % higher than the PREL values across the whole spectral range.

First, we mention that this relative difference is within the respective error bars of the KP and PREL measurements (see the Appendix). However, we need to determine whether
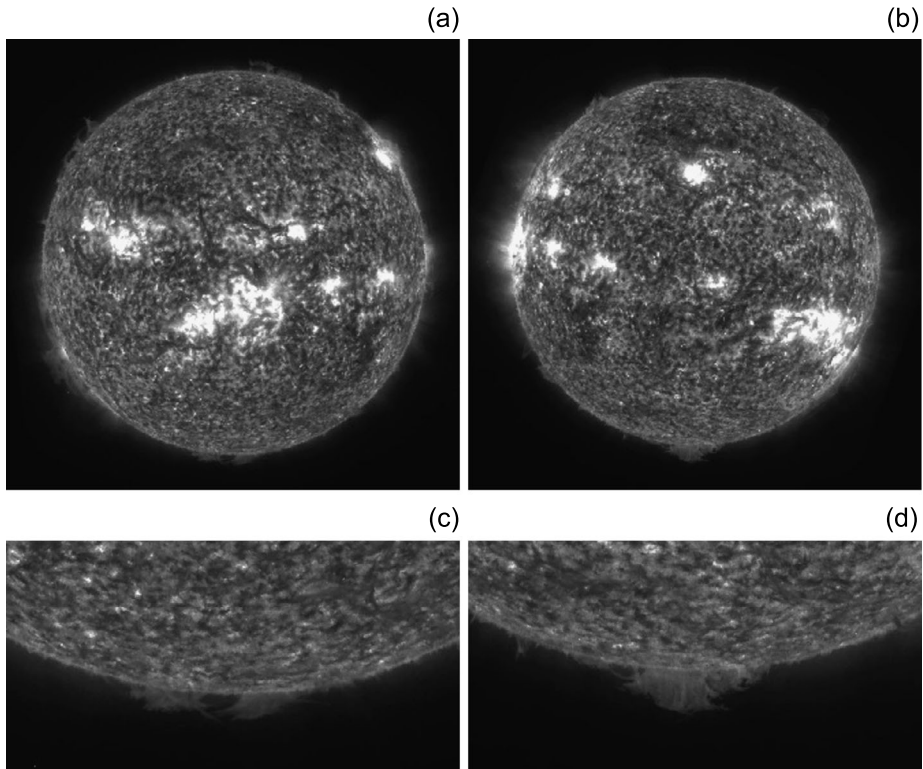
Figure 4 EUVI/STEREO images in He II 304 Å on 18 July 2013. (a) STEREO-A at 17:26:15. (b) STERE-O-B at 16:16:15. (c) Zoom on the south pole (STEREO-A). (d) Zoom on the south pole (STEREO-B). The size of the zoomed images is 480 × 240 arcsec.

there might be any systematic errors related to the two methods. The PREL shows a bias that can be considered a launch and post-launch degradation, an effect well-known in the far-UV – see *e.g.* Bonnet *et al.* (1978), or more recently Wilhelm *et al.* (2002) – but not so strong in the near-UV (Bonnet *et al.*, 1978). We discarded this possibility because of the closeness of the launch date. Moreover, the PREL calibration seems to provide almost the same quiet-Sun results as HRTS-9 at 2801 Å (Heinzel and Kleint, 2014).

We discuss hereafter possible sources of errors in our KP method. First of all, we verify whether our profiles at $\mu = 0.23$ on the solar disk are comparable to the KP profiles. We took great care to integrate on the same range of μ as KP (Figure 7) did, but we do have a better spatial resolution across the slit, which results in a high spatial variability that the averaging over μ does not eliminate. In this process, it is well possible that we selected fainter structures (more cells?) than KP did, and as a result, the PREL calibration provides lower values. We can also think of the presence of cool absorbing material, although the filament is located above 80° latitude and its projection is located well beyond $\mu = 0.23$ (and above the limb).

A third step consisted of using a method proposed by J.-P. Wuelser (private communication, 2015), which is based on a comparison between IRIS mosaic data and SOLSTICE (irradiance) data. This method, briefly discussed in the Appendix and called SOLS, provides a good agreement with KP for the ratio of k to h sensitivities, but (slightly) increases
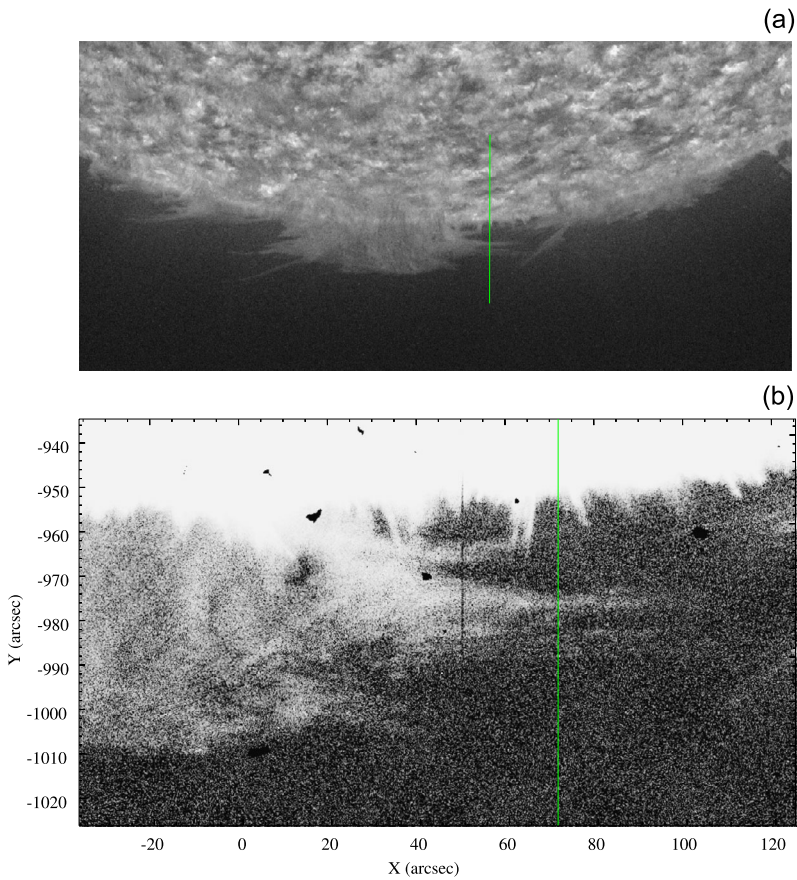
(a)

(b)

Figure 5 Position of the IRIS slit. (a) Position of the IRIS slit on the 304 Å AIA image at 17:27:43. The size of the image is 780×360 arcsec. (b) Zoom on the observed prominence and position of the slit (in green) corresponding to the Mg II h and k observations on a SJI in the C II channel; the two positions (black and green) correspond to the SJI physical slit and to the position of the slit when spectra are obtained: while we use SJI images from a time when the slit was at $X \approx 50$ arcsec, our spectra are from times when the slit was at $X \approx 70$ arcsec (green line). Note that the Mg II spectra were obtained from 17:27:53 to 17:28:03 and the SJI image at 17:28:29.

the absolute value disagreement with KP. SOLS certainly is the best method for observations made after the CCD bake-out (J.-P. Wuelser, private communication), but it leads to some uncertainties for our 18 July observations. In the absence of decisive argument, we chose to present the three results (Table 2), but selected the standard PREL calibration for the comparison with the models. We note that the above-mentioned discrepancy between the three methods might be overcome with many more disk-center and $\mu = 0.23$ measurements in quiet regions throughout Cycle 24.

4. Observation and Characterization of Threads in the Prominence

We selected the observations performed between 17:27 and 17:29 UT (Table 2), which have the advantage of a good signal-to-noise ratio (exposure time of 15 s), a clear separation

Figure 6 Calibrated profiles obtained in the vicinity of Mg II h and k lines at the $\mu = 0.23$ position on the solar disk. Red curve: pre-flight (PREL) calibration method. Green curve: calibration method using the quiet-Sun values of Kohl and Parkinson (1976, KP) as references.
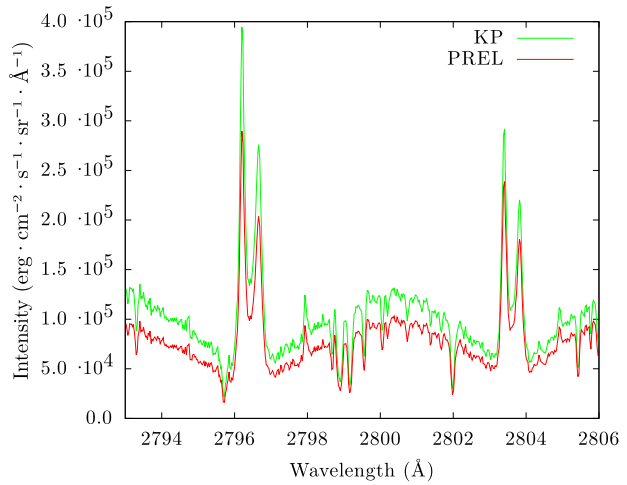

Table 2 Main parameters of the k and h profiles observed in regions A and B for PREL, KP, and SOLS calibrations. The error bars (which correspond to statistical uncertainties) are only provided for the PREL calibration values. I_k and I_h are given in $\mathrm{erg\,s^{-1}\,cm^{-2}\,sr^{-1}}$, I_{k_3} and I_{h_3}, the values at the center of the profiles, are given in $\mathrm{erg\,s^{-1}\,cm^{-2}\,sr^{-1}\,\mathring{A}^{-1}}$.

	Region A			Region B		
	PREL	KP	SOLS	PREL	KP	SOLS
I_k	6210 ± 450	8450	5480	2990 ± 315	4065	2635
I_h	4410 ± 390	5650	3700	2010 ± 260	2580	1690
I_k/I_h	1.41 ± 0.22	1.49	1.48	1.48 ± 0.35	1.57	1.56
I_{k_3}	36500 ± 6900	49630	32200	24610 ± 5665	33480	21710
I_{h_3}	27915 ± 6110	35810	23450	18120 ± 4920	23240	15220
FWHM(k) (Å)	0.16 ± 0.04	0.16	0.16	0.12 ± 0.04	0.12	0.12
FWHM(h) (Å)	0.15 ± 0.045	0.15	0.15	0.11 ± 0.04	0.11	0.11

between threads, and a line of sight (LOS) quasi-perpendicular to these elongated structures. We identified threads with the SJI (Figure 5) and also with the help of spatial cuts along the slit in the h and k intensities. Figure 7 shows spatial Mg II h and k cuts superimposed upon a simultaneous C II SJI. The bright C II ring is about cospatial with the bright h and k limb (spicule material), and the threads are clearly located above the chromosphere. The position and extension where the $\mu = 0.23$ profiles were computed are also shown in the Figure 7. The strong network/internetwork variability of the h and k intensities is clearly visible, which impacts the KP calibration as discussed in the Appendix. The weak emission in both C II and Mg II of the horizontal threads located about 30 arcsec above the limb is evident as well. The Mg II emission there is about one order of magnitude lower than on the disk. Figure 8 displays a focus on these tiny structures where three thread systems are located at positions 340, 290, and 270, respectively when moving out from the limb. We discarded the profile analysis at position 270 and focused first on position 340 (called hereafter A) and then on position 290 (called hereafter B).

Figure 7 Spatial cuts along the slit in the h (green) and k (red), integrated over 1 Å, calibrated intensities superimposed upon a simultaneous C II SJI. Spatial steps represent 1/6 arcsec and the origin is at the location of the photospheric limb. The rectangular blue box along the slit indicates the location of the $\mu = 0.23$ profiles obtained in the range $0.184 - 0.249$ corresponding to KP observations.
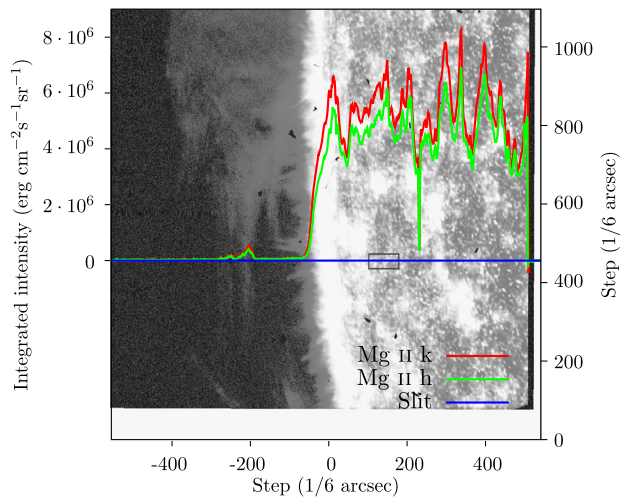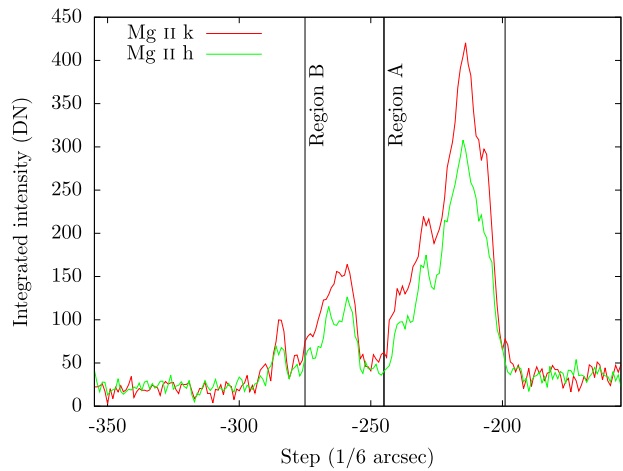
Figure 8 Cuts in the integrated (over 1 Å) intensities of Mg II k (red) and h (green), in count numbers, along the slit in the prominence region. Spatial steps represent 1/6 arcsec and the origin is at the location of the photospheric limb. The extensions of regions A (pixel 340) and B (pixel 290) are also shown.

4.1. Mean Profiles

We first worked on profiles averaged between positions 310 and 356 (A) and 280 and 301 (B). These profiles were corrected for stray light (a correction of about 3 %) and deconvolved from the instrumental profile (for which we adopted a 50 mÅ value, see De Pontieu *et al.* (2014) and J.-P. Wuelser (private communication)).

We noted that the deconvolution has a small effect on the profiles, which remain unreversed. We study the calibrated average profiles and compare them with profiles resulting from modeling in Section 5.

4.2. Spatial Variation of Mg II h and k Profiles

We wished to make full use of the high spatial resolution of IRIS to detect, if possible, the fine structure at positions A and B. We plot in Figure 9 the spatial variation of the Mg II k and h profiles along the slit at position A.
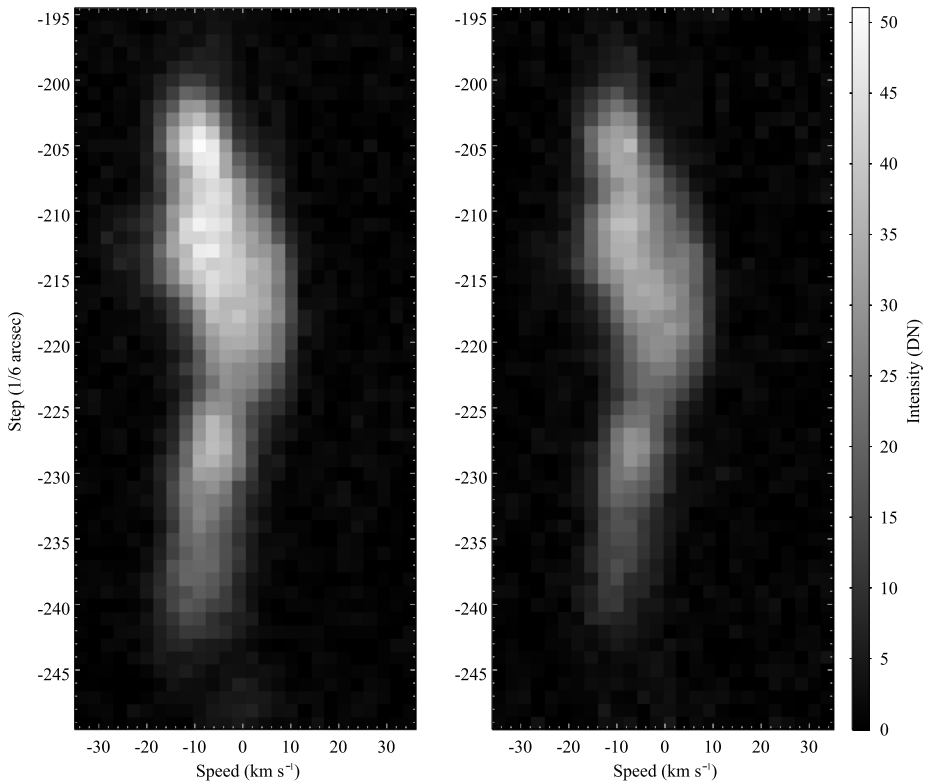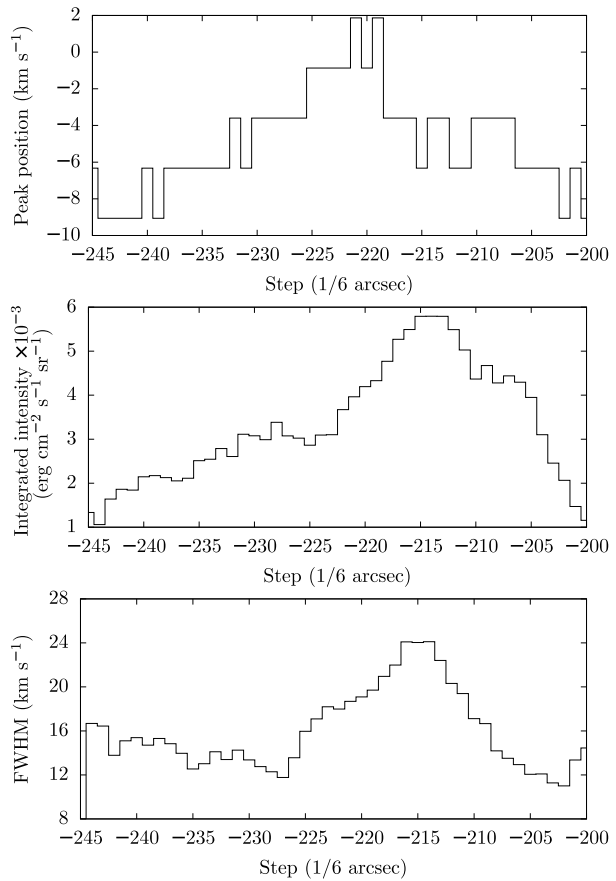
Figure 9 Spectra of Mg II k (left) and Mg II h (right) lines zoomed on region A. The wavelength shift has been converted to velocity (km s^{-1}), where negative velocities correspond to receding material along the LOS.

We note that the k and h profiles have similar line shifts from step to step. These shifts are compared with the line intensities (Figures 10 and 11) only for k in regions A and B, respectively (h results are similar).

The line redshift (about 0.1 Å) corresponds to both edges of structure A, and the region of maximum of intensity displays a low velocity. This redshift at the edges implies a motion along the line of sight away from the observer of about 9 km s^{-1}. Similar values have been obtained at the external boundaries (or envelopes) of prominences in the Ca II K and H lines (Vial, 1982) and in the Hα line (Mein, 1977). For low-resolution observations, it has generally been agreed that they correspond to actual flows. In our case (see the geometry in Figure 5b), the thread system is roughly located in the plane of sky (another geometry would imply very elongated structures perpendicular to the prominence inversion line (PIL)) in such a way that the LOS is closer to the perpendicular to the threads. Consequently, this redshift could only correspond either to very strong flows along the threads or to a transverse oscillation (since the exposure time is short enough compared with periods longer than three minutes). (For the latest review, see Ballester, 2015). Moreover, Figure 10 shows that the un-shifted profiles are broader than the shifted profiles, which was previously noted by Engvold, Wiehr, and Wittmann (1980). The results for region B (Figure 11) clearly show that the (small) variations of velocity and FWHM are at the limits of the statistical accuracies.

This could result from the superposition of narrow shifted profiles, as in Schmieder *et al.* (2014). This interpretation is supported by the comparison between the different behaviors of the FWHM in regions A and B. In region A, the large FWHM corresponds to a superposition of small threads providing each narrow profile. These narrow profiles can be distinguished in region B.

5. Comparison Between Typical Mg II Calibrated Profiles and Modeling

We present for region A the Mg II k and h calibrated profiles (with PREL and KP methods) in Figure 12.

We now compare the main parameters of these profiles with those of the profiles resulting from one-dimensional modeling (Heinzel, Vial, and Anzer, 2014), in particular their Table 2. The observational results are summarized in Table 2.

Because of the high resolution of IRIS observations, we considered the lowest values of the k intensity in Table 2 of Heinzel, Vial, and Anzer (2014), which correspond unequivocally to the models with the smallest thickness (200 km). When the same thickness (200 km) at low temperatures (6000 K) is maintained, the profiles are unreversed at all pressures (up to 0.5 dyn cm^{-2}). At higher temperatures (8000 K and 10 000 K), only the smallest pressure

Figure 11 Shift of the center of Mg II k profile along the slit in region B converted to km s^{-1} (top) compared to the variation of the Mg II k line intensity along the slit in region B (middle) (method PREL) and the variation of the FWHM along the slit in region B in pixel (bottom). Note that the zero velocity corresponds to the center of the profile reversals at the extreme limb (Figure 6).
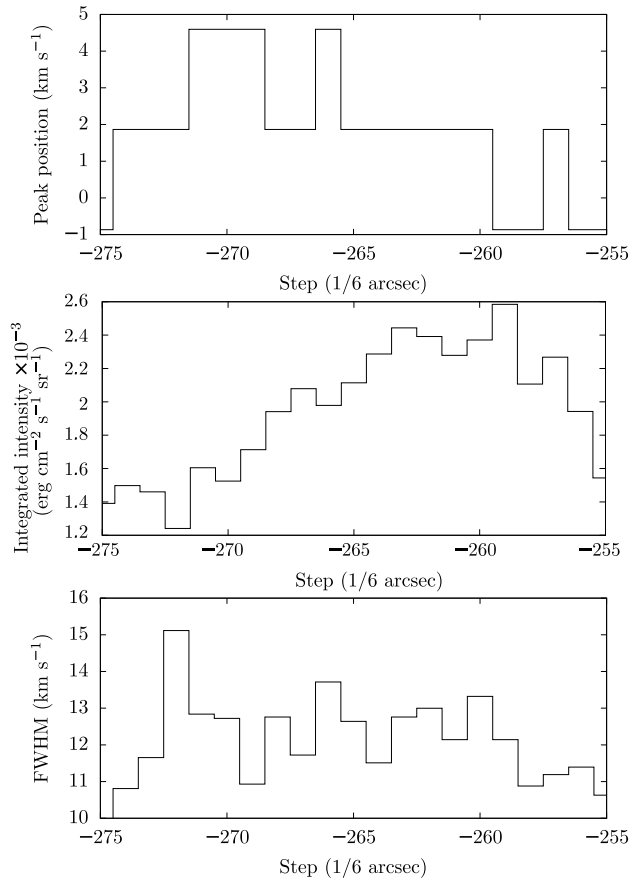
(0.01 dyn cm^{-2}) allows for a non-reversal. When the thickness increases, it becomes more and more difficult to find unreversed profiles until a thickness of 5000 km only provides reversed profiles.

   To distinguish between the different models, we now consider the absolute intensities of the k and h lines. Our k value of 6210 (region A, PREL) would match the models with the lowest pressure value (0.01 dyn cm^{-2}) for a temperature range of 6000 – 10 000 K. The k_3 observed value (3.65×10^4 erg s^{-1} cm^{-2} sr^{-1} Å^{-1}) also only matches the computed low-pressure values of about 10^{-7} erg s^{-1} cm^{-2} sr^{-1} Hz^{-1}. But for the h intensity value we note a large discrepancy between the observed intensity (4410) and the computed one (3700). (Note that the discrepancy is larger than the (statistical) error bar but stays within 2σ.) Moreover, these models with a very small thickness (200 km) do not match the geometry of the observed structures, whose extension in the plane of sky is about 5 arcsec (or 3500 km) for region A. However, we note that the geometrical thickness of the model is the effective thickness (the overall thickness of threads filled with material), which may be smaller than the apparent thickness because of a small filling factor.

   In region B only models with a still lower pressure (< 0.01 dyn cm^{-2}) or thickness (< 200 km) would match k values for a 6000 K temperature, but not the h values since the ratio k/h is about the same for regions A and B, *i.e.* well below 2.

Figure 12 Mean Mg II profiles.
From top to bottom : Mg II k in
region A, Mg II h in region A,
Mg II k in region B, and Mg II h
in region B.
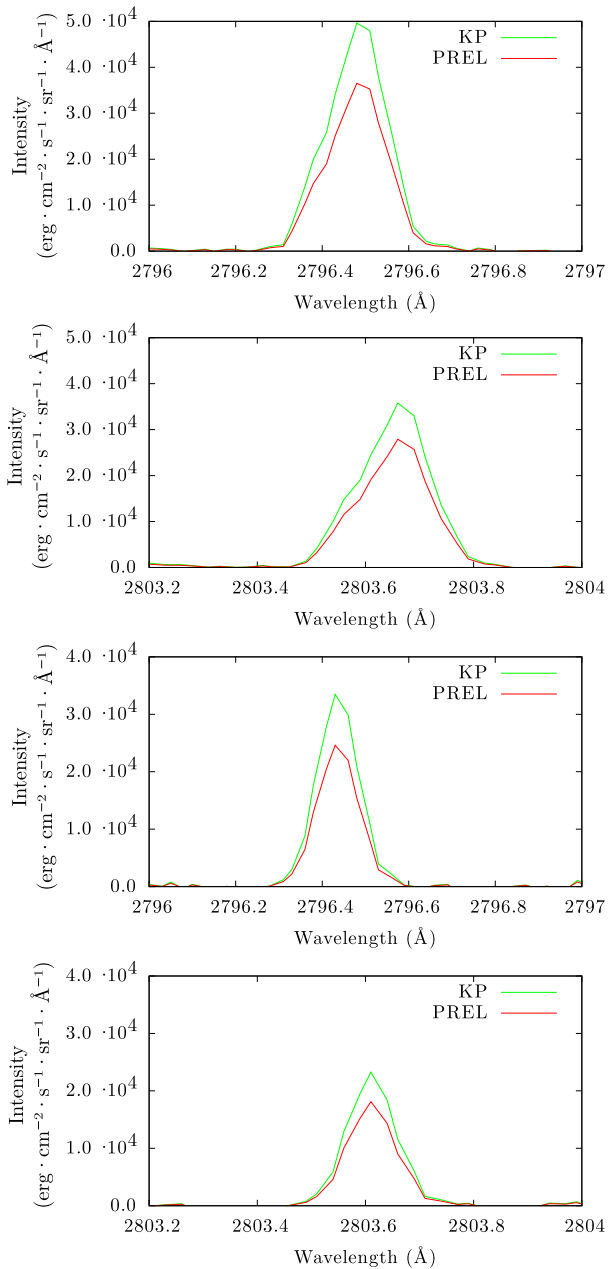
The KP values do not change the question of the h intensity discrepancy when a low
pressure and low thickness model is adopted for k. Both observed values of k/h (in the
range 1.4 – 1.6) and k_3/h_3 (about 1.35) could indicate a rather high opacity of the two lines,
which is not achieved with the above-mentioned models with small thickness and pressure.
But this possibility should be ruled out since it would translate into reversed strong pro-
files, which are not observed. The models discussed are simple 1D-slab models, which are

isothermal and isobaric. While the line-center opacity ratio between k and h lines is equal to two (the ratio of oscillator strengths), the computed intensity ratios vary from close to two for optically thin slabs to values of around 1.5 or lower for thick slabs. In the latter cases, the source function in the line core decreases to the slab surface, and this leads to reversed profiles. We note that Mg II line cores in prominence slabs are well reproduced with the complete frequency redistribution, as discussed by Heinzel, Vial, and Anzer (2014), who performed partial-redistribution modeling for all their slabs. Possible reasons for discrepancies between the line intensities and the line ratios are further discussed in Section 7, while in the following section we use complementary observations to understand these problems.

6. Complementary Observations

Hα: in the BBSO and Teide Hα images of Figure 2 the horizontal threads that we detected in the Mg II and C II channels are barely visible. Their intensities are not higher than about 100 counts (Figure 2a), while at disk center the intensity is about 2500 counts. The central intensity at disk center of the quiet Sun is 0.7×10^{-5} erg s^{-1} cm^{-2} sr^{-1} Hz^{-1} or 5×10^5 erg s^{-1} cm^{-2} sr^{-1} Å^{-1} or 1.25×10^5 erg s^{-1} cm^{-2} sr^{-1} over a bandpass of 0.25 Å. This results in an emission of 5×10^3 erg s^{-1} cm^{-2} sr^{-1} for regions A and B. According to the correlation plot of Gouttebroze, Heinzel, and Vial (1993, Figure 3), this provides an emission measure of about 10^{28} cm^{-5}. With a thickness of 3500 km for region A and 2900 km for region B, we can derive a mean electron density of about 6×10^9 cm^{-3} in the threads. Translated into pressure, this value is obviously beyond the lower values of Table 2 of Heinzel, Vial, and Anzer (2014). Such a low value could explain why the Hα emission is so weak. The opacity in the Hα line is typically lower than the opacity in the Mg II line by two orders of magnitude. However, we recall that the Hα filter bandpasses (0.25 Å for BBSO and 0.4 Å for Teide) correspond to about 11 and 18 km s^{-1}, which means that the Hα emission can easily go off-band when observing dynamic prominence features.

SJI C II and 1400 Å channels: although the threads are visible in Figures 1a and 5b, plotted in log scale, the very low signal at positions A and B (lower than 4 %) can only confirm the low-density values.

AIA 304 Å (level 1) data: The ratio $I_{\mathrm{prominence}}/I_{\mathrm{disk}}$ is about 0.43 (region A) and 0.26 (region B). The A value is easily explained by the very nature of the He II 304 Å emission at low density and temperature because in these conditions the emission is dominated by the resonance scattering of the incident chromospheric and transition-region line. The ratio is close to the dilution factor. The lower value in region B can be explained similarly, but either with a lower opacity or possibly with some radial velocity providing Doppler dimming (Labrosse *et al.*, 2010). However, we note that the two values of the ratio are known within 25 %.

7. Discussion

We have seen that models which combine small thickness (about 200 km) and pressure (about 0.01 dyn cm^{-2}) can explain the observed unreversed profiles and the low values of the Mg II h and k integrated intensities in regions A and B, but do not provide the low values of the ratio of k to h intensities. The low value of the k/h ratio has remained a puzzle since

the early studies in 1982, when Vial (1982) measured a value of 1.6 and continues at present, when Schmieder *et al.* (2014) found a value of 1.33. Various processes might lead to low values of the k and h intensities and of their ratio.

First, when the low Hα thread visibility is considered, the low h and k intensities can result from very low values of the density (and consequently the pressure), which were not explored in Table 2 of Heinzel, Vial, and Anzer (2014). However, most previous studies that combined observations and modeling in a wide range of lines (hydrogen, Mg II, Ca II, etc., see Labrosse *et al.*, 2010) derived low pressures (but higher than 0.01 dyn cm^{-2}). This does not solve the problem of the too low line ratios that are observed, however.

Second, an important attenuation of the emitted intensity can be obtained from the process called Doppler dimming, which results from plasmas submitted to predominantly radial velocities that absorb a Doppler-shifted radiation. To be efficient, it is required that the dominant emission process is the resonance scattering of incident chromospheric Mg II h and k line radiation and that the plasma is subjected to a strong vertical velocity field. The first condition is easily met at low densities ($< 10^{10}$ cm^{-3}, see Section 5) and at the typical temperatures of prominences ($< 10\,000$ K). The second condition requires very high velocities to be effective. For instance, a 100 km s^{-1} (or higher) velocity corresponds to a dimming factor of no less than 2.5 (Figure 9 of Heinzel, Vial, and Anzer, 2014). No such apparent radial velocity of the observed threads has been observed, and the thread sections are too small to enclose such an internal velocity field perpendicular to the field lines and its gradient.

Third, we consider the fine structure of prominences, in particular of the threads we observed. This issue has been addressed by Gunár *et al.* (2008), who developed 2D multi-thread models and successfully interpreted the hydrogen Lyman line profiles as observed by SOHO/SUMER (Gunár, 2014). However, these models could only play an important role in the differential h and k emission if they have well-separated threads, allowing for a full penetration of the incident chromospheric radiation. Since the chromospheric radiation will dominate the thermal source of the h and k photons, we still have a scenario where the k/h ratio is the k/h chromospheric ratio multiplied by the ratio of oscillator strengths. We are far from obtaining a k/h ratio of about 1.4 – 1.5.

Finally, the observed LOS velocities (of the order of 9 km s^{-1}) might be the LOS projection of strong flows along the threads. Preliminary 1D computations show that horizontal flows of about 100 km s^{-1} lead to a decrease of the k/h ratio. This can be obtained with either low-pressure and small-thickness models at low temperature, as mentioned above, or with low-pressure, medium-thickness and high-temperature models. For instance, a model with the observed thickness of region A (3000 km), a pressure of 0.01 dyn cm^{-2}, a 100 km s^{-1} flow and a temperature of 15 000 K provides a k/h ratio of 1.45. This means that there are two paths for the solution: either a very thin model (less than 200 km) and a low temperature: this leads to a small filling factor (less than 0.1 across the layer), or a thick model (with a filling factor close to 1) at high temperature (at least 10 000 K). All of them require a low pressure (about 0.01 dyn cm^{-2}). Horizontal flows of about 100 km s^{-1} will not affect the line source function for an ideal case of 90 deg scattering, but in reality, we integrate the incident radiation from all incoming directions, and thus flows have a certain effect that is due to the projection of the flow velocity into the direction of the incident radiation (this effect increases with decreasing height above the solar surface). If such a projected velocity is lower than about 20 km s^{-1}, we might be studying Doppler brightening instead of dimming – see Figure 9 in Heinzel, Vial, and Anzer (2014). However, this kind of brightening will be different for k and h lines, depending on the actual gradient of the incident line intensity in the chromospheric line core. Furthermore,

these line-core intensities and gradients vary substantially during the solar cycle, but also across the solar disk due to its inhomogeneities. For instance, Heinzel, Vial, and Anzer (2014) have used the incident Mg II line radiation according to the observed line profiles of Staath and Lemaire (1995), but these profiles exhibit different line-core gradients than quiet-Sun profiles from current IRIS observations. A similar problem with different gradients can play a role in the outer parts of the line peaks and inner wings for the case of Doppler dimming. We conclude that the only way to solve the problem is to compute the NLTE radiative transfer in various 2D structures representing long thin threads with internal flows. To compare them with the IRIS spectra, it will be necessary to use as the incident radiation the quiet-Sun Mg II h and k line profiles observed by IRIS in times close to prominence observations. This systematic modeling will be our next task.

On the observational side, it is also important to accumulate prominence Mg II observations of various structures seen from different viewing angles, including the central parts of prominences, and to focus on the absolute intensities of Mg II k and h (and their ratio).

Appendix: IRIS NUV Photometric Calibration – A Comparison Between the Pre-launch Calibration Method and Independent Methods

A.1 Introduction

Photometric calibration of space instruments, especially in the UV, is a tricky problem (see *e.g.* Huber *et al.*, 2013). Since the on-board implementation of a stable absolute source is often impossible, solar physicists have to rely upon pre-launch measurements on the ground, which are not only difficult in the UV, but may prove unreliable because of inevitable on-orbit degradation (for a dramatic case, see Lemaire, 1991). IRIS provides a calibration tool (De Pontieu *et al.*, 2014) that is based on pre-launch measurements and probably is a good approximation since our observations took place immediately after IRIS was operating. However, we also implemented an ancillary photometric calibration method that does not depend on the pre-launch calibration. It relies upon IRIS observations of a quiet solar region at a location where Mg II data have been obtained and carefully calibrated previously (Kohl and Parkinson, 1976). It has been extensively used by most post-KP Mg II studies (Staath and Lemaire, 1995; Gurman, 1984). Moreover, we also compared the absolute intensities obtained with the two methods, with a third method that relies upon full-disk IRIS and SOLSTICE measurements (Wuelser, private communication).

A.2 Method

From IRIS Level 1.5 data (see De Pontieu *et al.* (2014) for data level definition) we computed integral intensities under Mg II k and h lines near the limb (over 1 Å) as well as specific features (k_{1r}, k_{2v}, k_{2r}, k_3, h_{1v}, h_{1r}, h_{2v}, h_{2r}, and h_3) and compared them to the values measured by Kohl and Parkinson (1976) from a near-limb ($\mu = \cos\theta = 0.23$) quiet region. We assumed that the region our IRIS spectrum was taken from (slit-center at 70 arcsec, −943 arcsec) had the same quiet-Sun characteristics as the observed region (Kohl and Parkinson, 1976).

A.2.1 Data

Using data close to the limb required carefully defining the proper limb and solar radius. The limb was defined by the inflection point at 2832 Å. We then used IRIS spatial calibration and ephemeris verification to determine the Sun's angular radius at the observation date (944.25″), and then associated a μ value to each pixel of the near-UV (NUV) spectrum.

To reduce noise, we computed a mean intensity profile for μ within the $0.184 - 0.249$ range from IRIS level 1.5 NUV uncalibrated data. This range is the interval where μ could vary along the slit in Kohl and Parkinson's rocket measurements. (We also performed a calibration with the worst variation bounds that Kohl and Parkinson (1976) reported for μ and found very similar results.) All data we later compared to Kohl and Parkinson's were measured from this mean profile.

A.2.2 Conversion Factor Computation

By comparing integrated intensities (in DN) computed from our mean profile under Mg II h and k lines with Kohl and Parkinson's measurements, we were able to determine a first pair of conversion factors (one for k and one for h). IRIS data were then converted from DN into absolute units (namely CGS system units).

We performed the same comparison with specific features on each line profile (what Kohl and Parkinson (1976) called *inflection points*) and determined a second pair of conversion factors, each being the average of conversion factors computed for all featured points of the line.

Because of the Mn I absorption line in the blue wing of Mg II k, k_{1v} was omitted.

The average result of the preceding methods drew two conversion factors, one for each line, to which we refer to as α_k and α_h.

A.2.3 IRIS' Sensitivity Difference at Mg II k and h

As these two conversion factors were slightly different, we decided to have the conversion factor depend on the wavelength. At wavelengths shorter than Mg II k we used α_k, between Mg II k and Mg II h we used a linear interpolation between α_k and α_h, and at wavelengths longer than Mg II h we used α_h.

As a result, this calibration method is only efficient near the Mg II doublet. Since our present analyses focus on the Mg II k and h lines, this precision is satisfactory.

Figure 13 Calibrated data comparison: Mg II k line profile at $\mu = 0.23$. The dashed line represents IRIS pre-launch calibrated data, while the solid line represents data computed using factors from our KP comparison.
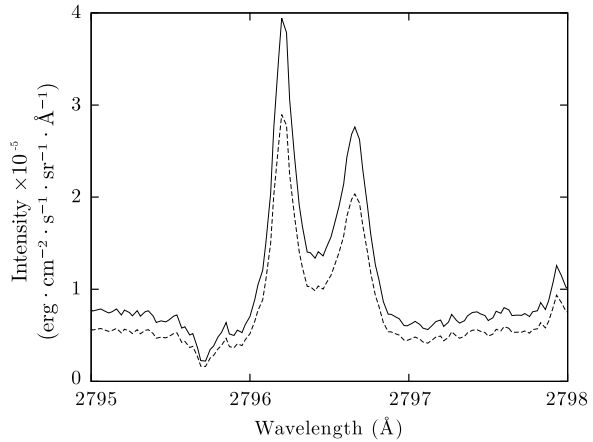
A.3 Results and Comparison with Pre-launch Calibration

This method yields calibrated data whose values are on average 28 % higher than IRIS Level 2 corresponding data. We discuss this difference in Section A.4. An example is given in Figure 13.

In addition, we found that IRIS NUV spectrometer is 3.4 % more sensitive in the Mg II h line than in the Mg II k line, while the pre-launch calibration provides an opposite 2.7 % difference between k and h.

In Section A.2.2 we have made the arbitrary choice of using all featured points regardless of their reliability. We also used k_{1r}, h_{1v}, and h_{1r} only because even though they are much more affected by noise, their values are less dependent on solar activity. Using only these three points led to a 25 % difference with the pre-launch calibration, but this came with a sensitivity difference of 8.8 % between k and h lines. A global sensitivity change between pre-launch calibrations and observations being much more likely than an increase in sensitivity difference, we chose to use all featured points for our calibration.

A.4 Uncertainty

Kohl and Parkinson's values are accurate to $+12$ %/-20 % for k_1 and h_1 points, and to ± 12 % for other data we used. If we assume a $\sqrt{N}$ statistical uncertainty on IRIS uncalibrated data, our calibration method should be accurate to $+16$ %/-17 %. Consequently, the proposed pre-launch value is within the combined KP and IRIS error bars.

The method relies on the assumption that the region of the Sun Kohl and Parkinson observed *and* the region IRIS data are taken from are similar quiet regions at different epochs of different solar cycles, however.

A.5 A Complementary Method

Since one can assemble a full-disk mosaic from many individual IRIS observations, it is possible to compare its values with the SOLSTICE irradiance values (J.-P. Wuelser, private communication). A preliminary investigation by J.-P. Wuelser (private communication) shows that the effective area seems to be less wavelength dependent and in fact behaves oppositely to the pre-launch measurements near the Mg II lines (Figure 14).
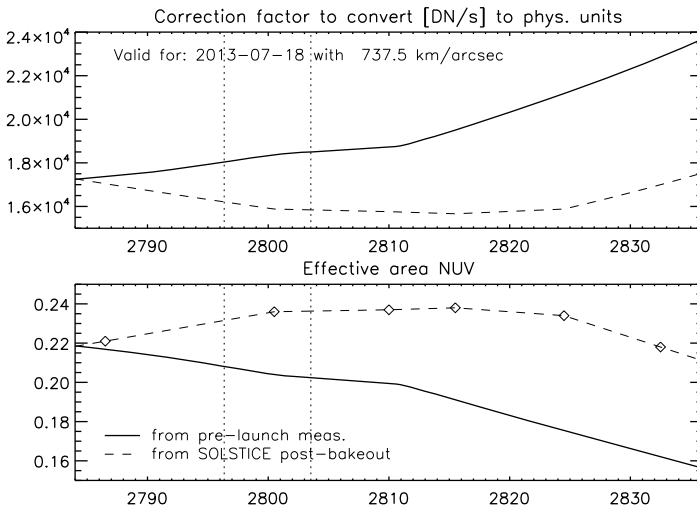
Figure 14 Comparison of the IRIS photometric sensitivities derived from pre-launch measurements (full line) and derived from SOLSTICE irradiance (dashed line). Top: conversion factor from DN s^{-1} to cgs physical units. Bottom: effective area. Abscissae: wavelength in (Å).

After the CCD bake-out, the SOLSTICE method provides values lower by about 12 % than were obtained before launch, but this indicates that the h sensitivity is higher by 2.5 % than the k sensitivity, which better agrees with the 3.4 % value from the Kohl and Parkinson method. Because the comparison with SOLSTICE was made in late 2014, it is unclear whether the spectral behavior is different for our 2013 measurements or whether the effective areas should be corrected to take the degraded throughput into account. A thorough comparison of the three methods over a long time span (on the order of one cycle) is certainly necessary.

References

Ballester, J.L.: 2015, Magnetism and dynamics of prominences: MHD waves. In: Vial, J.-C., Engvold, O. (eds.) *Solar Prominences*, Springer, Berlin 259. DOI. ADS.

Bonnet, R.M., Blamont, J.E., Gildwarg, P.: 1967, Limb-darkening observations from 1800 to 2800 Å. *Astrophys. J. Lett.* **148**, L115. DOI. ADS.

Bonnet, R.M., Lemaire, P., Vial, J.C., Artzner, G., Gouttebroze, P., Jouchoux, A., Vidal-Madjar, A., Leibacher, J.W., Skumanich, A.: 1978, The LPSP instrument on OSO 8. II – In-flight performance and preliminary results. *Astrophys. J.* **221**, 1032. DOI. ADS.

De Pontieu, B., Title, A.M., Lemen, J.R., Kushner, G.D., Akin, D.J., Allard, B., Berger, T., Boerner, P., Cheung, M., Chou, C., Drake, J.F., Duncan, D.W., Freeland, S., Heyman, G.F., Hoffman, C., Hurlburt, N.E., Lindgren, R.W., Mathur, D., Rehse, R., Sabolish, D., Seguin, R., Schrijver, C.J., Tarbell, T.D., Wülser, J.-P., Wolfson, C.J., Yanari, C., Mudge, J., Nguyen-Phuc, N., Timmons, R., van Bezooijen, R., Weingrod, I., Brookner, R., Butcher, G., Dougherty, B., Eder, J., Knagenhjelm, V., Larsen, S., Mansir, D., Phan, L., Boyle, P., Cheimets, P.N., DeLuca, E.E., Golub, L., Gates, R., Hertz, E., McKillop, S., Park, S., Perry, T., Podgorski, W.A., Reeves, K., Saar, S., Testa, P., Tian, H., Weber, M., Dunn, C., Eccles, S., Jaeggli, S.A., Kankelborg, C.C., Mashburn, K., Pust, N., Springer, L., Carvalho, R., Kleint, L., Marmie, J., Mazmanian, E., Pereira, T.M.D., Sawyer, S., Strong, J., Worden, S.P., Carlsson, M., Hansteen, V.H., Leenaarts, J., Wiesmann, M., Aloise, J., Chu, K.-C., Bush, R.I., Scherrer, P.H., Brekke, P., Martinez-Sykora, J., Lites, B.W., McIntosh, S.W., Uitenbroek, H., Okamoto, T.J., Gummin, M.A., Auker, G., Jerram, P., Pool, P., Waltham, N.: 2014, The Interface Region Imaging Spectrograph (IRIS). *Solar Phys.* **289**, 2733. DOI. ADS.

Doschek, G.A., Feldman, U.: 1977, High-resolution spectra of the solar Mg II h and k lines from SKYLAB. *Astrophys. J. Suppl.* **35**, 471. DOI. ADS.

Engvold, O., Wiehr, E., Wittmann, A.: 1980, The influence of spatial resolution on the Ca⁺K line width and shift in a quiescent prominence. *Astron. Astrophys.* **85**, 326. ADS.

Gouttebroze, P., Heinzel, P., Vial, J.C.: 1993, The hydrogen spectrum of model prominences. *Astron. Astrophys. Suppl.* **99**, 513. ADS.

Gunár, S.: 2014, Modelling of quiescent prominence fine structures. In: Schmieder, B., Malherbe, J.-M., Wu, S.T. (eds.) *Nature of Prominences and Their Role in Space Weather*, *IAU Symp.* **300**, 59. DOI. ADS.

Gunár, S., Heinzel, P., Anzer, U., Schmieder, B.: 2008, On Lyman-line asymmetries in quiescent prominences. *Astron. Astrophys.* **490**, 307. DOI. ADS.

Gunár, S., Schwartz, P., Schmieder, B., Heinzel, P., Anzer, U.: 2010, Statistical comparison of the observed and synthetic hydrogen Lyman line profiles in solar prominences. *Astron. Astrophys.* **514**, A43. DOI. ADS.

Gurman, J.B.: 1984, The Mg II h line in sunspot umbrae. *Solar Phys.* **90**, 13. DOI. ADS.

Heasley, J.N., Mihalas, D.: 1976, Structure and spectrum of quiescent prominences – Energy balance and hydrogen spectrum. *Astrophys. J.* **205**, 273. DOI. ADS.

Heinzel, P., Kleint, L.: 2014, Hydrogen Balmer continuum in solar flares detected by the Interface Region Imaging Spectrograph (IRIS). *Astrophys. J. Lett.* **794**, L23. DOI. ADS.

Heinzel, P., Vial, J.-C., Anzer, U.: 2014, On the formation of Mg II h and k lines in solar prominences. *Astron. Astrophys.* **564**, A132. DOI. ADS.

Heinzel, P., Schmieder, B., Mein, N., Gunár, S.: 2015, Understanding the Mg II and Hα spectra in a highly dynamical solar prominence. *Astrophys. J. Lett.* **800**, L13. DOI. ADS.

Huber, M.C.E., Pauluhn, A., Culhane, J.L., Timothy, J.G., Wilhelm, K., Zehnder, A. (eds.): 2013, *Observing Photons in Space: A Guide to Experimental Space Astronomy*, Springer, Berlin. ADS.

Kohl, J.L., Parkinson, W.H.: 1976, The MG II H and K lines. I – Absolute center and limb measurements of the solar profiles. *Astrophys. J.* **205**, 599. DOI. ADS.

Labrosse, N., Heinzel, P., Vial, J.-C., Kucera, T., Parenti, S., Gunár, S., Schmieder, B., Kilper, G.: 2010, Physics of solar prominences: I – Spectral diagnostics and non-LTE modelling. *Space Sci. Rev.* **151**, 243. DOI. ADS.

Lemaire, P.: 1991, Sensitivity changes in the CNRS ultraviolet spectrometer aboard OSO-8. *ESA J.* **15**, 237. ADS.

Lemaire, P., Skumanich, A.: 1973, Magnesium II doublet profiles of chromospheric inhomogeneities at the center of the solar disk. *Astron. Astrophys.* **22**, 61. ADS.

Lemen, J.R., Title, A.M., Akin, D.J., Boerner, P.F., Chou, C., Drake, J.F., Duncan, D.W., Edwards, C.G., Friedlaender, F.M., Heyman, G.F., Hurlburt, N.E., Katz, N.L., Kushner, G.D., Levay, M., Lindgren, R.W., Mathur, D.P., McFeaters, E.L., Mitchell, S., Rehse, R.A., Schrijver, C.J., Springer, L.A., Stern, R.A., Tarbell, T.D., Wuelser, J.-P., Wolfson, C.J., Yanari, C., Bookbinder, J.A., Cheimets, P.N., Caldwell, D., Deluca, E.E., Gates, R., Golub, L., Park, S., Podgorski, W.A., Bush, R.I., Scherrer, P.H., Gummin, M.A., Smith, P., Auker, G., Jerram, P., Pool, P., Soufli, R., Windt, D.L., Beardsley, S., Clapp, M., Lang, J., Waltham, N.: 2012, The Atmospheric Imaging Assembly (AIA) on the Solar Dynamics Observatory (SDO). *Solar Phys.* **275**, 17. DOI. ADS.

Mein, P.: 1977, Multi-channel subtractive spectrograph and filament observations. *Solar Phys.* **54**, 45. DOI. ADS.

Morrill, J.S., Korendyke, C.M.: 2008, High-resolution center-to-limb variation of the quiet solar spectrum near Mg II. *Astrophys. J.* **687**, 646. DOI. ADS.

Schmieder, B., Tian, H., Kucera, T., López Ariste, A., Mein, N., Mein, P., Dalmasse, K., Golub, L.: 2014, Open questions on prominences from coordinated observations by IRIS, Hinode, SDO/AIA, THEMIS, and the Meudon/MSDP. *Astron. Astrophys.* **569**, A85. DOI. ADS.

Staath, E., Lemaire, P.: 1995, High resolution profiles of the Mg II h and Mg II k lines. *Astron. Astrophys.* **295**, 517. ADS.

Tandberg-Hanssen, E.: 1995, *The Nature of Solar Prominences*, Springer, Berlin, 85. ADS.

Vial, J.C.: 1982, Optically thick lines in a quiescent prominence – Profiles of Lyman-alpha, Lyman-beta (H I), K and H (Mg II), and K and H (Ca II) lines with the OSO 8 LPSP instrument. *Astrophys. J.* **253**, 330. DOI. ADS.

Vial, J.-C., Engvold, O. (eds.): 2015, *Solar Prominences*, Springer, Berlin. DOI. ADS.

Wilhelm, K., Schuhle, U., Curdt, W., Dammasch, I.E., Hollandt, J., Lemaire, P., Huber, M.C.E.: 2002, Solar vacuum-ultraviolet radiometry with SUMER. In: Pauluhn, A., Huber, M.C.E., von Steiger, R. (eds.) *ISSI Scientific Reports Series* **2**, Springer, Berlin, 145. ADS.

Wuelser, J.-P., Lemen, J.R., Tarbell, T.D., Wolfson, C.J., Cannon, J.C., Carpenter, B.A., Duncan, D.W., Gradwohl, G.S., Meyer, S.B., Moore, A.S., Navarro, R.L., Pearson, J.D., Rossi, G.R., Springer, L.A., Howard, R.A., Moses, J.D., Newmark, J.S., Delaboudiniere, J.-P., Artzner, G.E., Auchere, F., Bougnet,

M., Bouyries, P., Bridou, F., Clotaire, J.-Y., Colas, G., Delmotte, F., Jerome, A., Lamare, M., Mercier, R., Mullot, M., Ravet, M.-F., Song, X., Bothmer, V., Deutsch, W.: 2004, EUVI: The STEREO-SECCHI Extreme Ultraviolet Imager. In: Fineschi, S., Gummin, M.A. (eds.) *Telescopes and Instrumentation for Solar Astrophysics, Proc. SPIE*, **5171**, 111. DOI. ADS.